Applied Mathematical Modelling 77 (2020) 810–828

Contents lists available at ScienceDirect

Applied Mathematical Modelling

journal homepage: www.elsevier.com/locate/apm

Method of characteristics for transient, spherical flows

Alan E. Vardy[a], Arris S. Tijsseling[b,*]

[a] School of Science and Engineering, University of Dundee, Dundee DD1 4HN, UK
[b] Department of Mathematics and Computer Science, Eindhoven University of Technology, P.O. Box 513, 5600 MB Eindhoven, The Netherlands

ARTICLE INFO

Article history:
Received 30 January 2019
Revised 2 July 2019
Accepted 23 July 2019
Available online 29 July 2019

Keywords:
Spherically-symmetric flow
Wave radiation
Wave reflection
Method of characteristics
Vibrating sphere acoustics

ABSTRACT

The equations of motion for spherically-symmetric, unsteady, inviscid, compressible flow are expressed in a form that enables accurate numerical solutions to be obtained using a one-dimensional formulation based on the method of characteristics. Unlike the corresponding equations for uniaxial unsteady flows, the spherically-symmetric equations necessarily include terms involving the reciprocal of the radius and, close to the radial origin, numerical integration is unreliable. Nevertheless, good accuracy is obtained over a wide range of radii, including regions inside the range where the pressure and acceleration are approximately in phase. The range of validity of the method is assessed by comparison with an analytical solution for a single pulse and the method is then used to predict the radiation of acoustic waves from the exit of a duct in which a pulse is propagating internally. A method of obtaining efficient solutions of flows containing both uniaxial and spherically-symmetric domains is then obtained. Interfaces between the domains are solved in a manner that ensures continuity of pressure and flowrate. The use of spherically-symmetric assumptions limits the range of three-dimensional domains that can be approximated, but the combination of the two forms of one-dimensional analysis makes highly efficient use of resources. Furthermore, the two-way coupling is a significant advantage over two-step methods that use independent solutions of the internal, uniaxial domain to provide prescribed boundary conditions for solutions of the external domain.

1. Introduction

Transient fluid flows exhibit features that are not present in steady flows, namely waves propagating in space-time. In the case of strong transients – herein implying 'sudden' rather than 'large' – the local behaviour of a flow experiencing wave action is usually dominated by inertial effects. The influence of molecular viscosity-related effects is much smaller than in most steady or slowly varying flows. This difference has a major influence on the key requirements of numerical methods suitable for studying particular types of flow. Another important influence on the choice of numerical methods is the geometry of the computational domain. When this is strongly three-dimensional, the only way forward involves the use of CFD methods that, even with modern computing resources can be highly time consuming. In many flows of high practical interest, however, the geometry can reasonably be approximated as uni-directional. Indeed, acceptable accuracy is often achievable by further approximating the conditions as one-dimensional.

* Corresponding author.
E-mail address: a.s.tijsseling@tue.nl (A.S. Tijsseling).

https://doi.org/10.1016/j.apm.2019.07.037
0307-904X/

List of symbols

A	coefficient in Eq. (5.5)
a	radius of sphere [m]
C	source term in the continuity equation Eq. (2.1) [kg/m s]
c	speed of sound [m/s]
f	frequency of excitation [Hz]; RHS in Eq. (1.1)
K	bulk modulus [Pa]
M	source term in the momentum equation Eq. (2.2) [kg/s^2]
MOC	method of characteristics
p	absolute pressure [Pa]
p'	gauge/acoustic pressure ($p' = p - p_0$) [Pa]
Q	volumetric flowrate [m^3/s]
$\dot{Q}$	rate of change of volumetric flowrate [m^3/s^2]
R	duct radius [m]
R_{gas}	specific gas constant [J/kg K]
r	spherical radial coordinate [m]
T	absolute temperature [K]
t	time coordinate [s]
u_r	velocity component in r direction [m/s]
u_x	velocity component in x direction [m/s]
x	axial coordinate [m]

Greek characters

γ	ratio of principal specific heat capacities [dimensionless]
λ	wavelength [m]
ρ	mass density [kg/m^3]
τ	indicative wave period [s]

Suffices

0	initial (ambient) conditions
a	innermost radius of external flow domain
r	radial component
x	axial component

For the particular case of transient flows such as water-hammer in long pipes, it is usually acceptable to make use of numerical methods that are especially well-suited to the analysis of inviscid, one-dimensional flow and that can be adapted to be of good accuracy even when allowing for complicating factors such as fluid friction. The method of characteristics (MOC) is especially important in this regard because it enables the equations of inviscid, one-dimensional, transient flow to be expressed as ordinary differential equations that can be integrated *exactly* at least in regions between boundaries and sometimes even in the presence of boundaries. Partly for this reason, the method has been the backbone of a huge volume of literature on the study of unsteady flows in conduits. The existence of source terms to represent complications such as friction and spatial variations of the flow cross-sectional area precludes the possibility of obtaining exact solutions for practical applications, but errors due to these terms can be constrained by, for instance, using sufficiently small grid sizes.

Typically, the use of one-dimensional methods to simulate transient flows in ducts is highly reasonable remote from boundaries, but it is less reasonable close to boundaries because three-dimensional flow patterns usually exist. In many applications, these 3-D zones are so short in comparison with duct lengths that they can be approximated in a one-dimensional manner without significantly downgrading the value of predictions. However, when the distance between two boundaries is only a few duct diameters, distortions of waves as a result of multi-directional flow can have a significant cumulative influence on interactions as the waves propagate back and forth. Often, this carries the potential risk of necessitating 3-D methods of analysis, but there is one special case for which the one-dimensional consequences of 3-D behaviour can be approximated quite well, namely wave reflection at a duct termination. Rudinger [1] analysed this case and provided a table of weighting factors that can be used in 1-D analyses to mimic delays in the reflection process. The present paper also considers this case, but takes it a step further. In addition to simulating wave reflections, resulting disturbances in the external environment beyond the duct exit are simulated. This can be relevant to a range of applications such as firearms, musical instruments, bird scares [2], vehicle exhaust systems [3] and even railway tunnels [4]. In each of these cases, the principal interest is in audible frequencies.

The great advantage of MOC for simulations of transient, one-dimensional flows does not normally exist for transient, two- or three-dimensional flows. This is because the characteristic transformation yields a reduction of only one in the overall number of independent variables. Thus, for a transient, three-dimensional flow, for example, the reduction is from

four (x, y, z, t) to three whereas for transient, one-dimensional flow, the reduction is from two to one. However, there are two special cases for which a reduction to only one spatial coordinate is possible, namely axially-symmetric and spherically-symmetric flows. In these cases, it is possible to cast the governing equations into ordinary differential forms and hence to integrate the differential terms exactly in sufficiently simple flows. Nevertheless, in contrast with the axial one-dimensional case, the resulting compatibility equations always include source terms, even in the simplest possible case with inviscid flow. Moreover, some of these terms tend to infinity as the radial coordinate tends to zero so there are important geometrical limitations on the applicability of simple numerical representations of the equations. The challenge for an analyst needing to undertake large numbers of simulations (e.g., for design optimisation or uncertainty quantification) is to find suitable ways of constraining the importance of these source terms. One way of achieving this is presented below.

1.1. Method of characteristics

MOC has been used outwith fluid mechanics [5–9], but attention herein is restricted to fluid acoustics. In this context, the most common applications in the case of spherically symmetric flows relate to bubble dynamics [10,11] and blast or shock waves [12–16]. In all cases that the authors have found, the ordinary differential equations have been expressed in a form that may be written generically as

$$\frac{dp}{dt} \pm \rho c \frac{du_r}{dt} = f_r\{r, u_r\} \tag{1.1}$$

where p = pressure, ρ = density, c = speed of sound, u_r = radial velocity, r = radial coordinate and t = time coordinate. This pair of equations is valid in the characteristic directions

$$\frac{dr}{dt} = u_r \pm c \tag{1.2}$$

respectively.

This is an appealing formulation because it closely resembles the one-dimensional form of MOC equations for uni-directional axial flows, namely

$$\frac{dp}{dt} \pm \rho c \frac{du_x}{dt} = f_x\{x, u_x\} \tag{1.3}$$

$$\frac{dx}{dt} = u_x \pm c \tag{1.4}$$

in which u_x = mean axial velocity and x = axial coordinate. Indeed, the similarity is commonly used to illustrate an important feature of spherically-symmetric transient flows, namely that the equations approach their axial flow counterparts asymptotically at large radii provided that the sources terms tend to zero.

For future reference, it is important to note that the close resemblance between the two sets of equations is somewhat misleading because there are important differences between the functions $f_r\{r, t\}$ and $f_x\{x, t\}$. In the uniaxial case, the function is zero in sufficiently simple cases. In contrast, its spherical counterpart, $f_r\{r, t\}$, can reduce to zero only in the limiting condition as the radius approaches infinity. This difference is addressed again below.

One particular manifestation of spherical flows is flow in a tapered tube [17]. With sufficiently gentle tapers, such flows can be analysed using Eqs. (1.3) and (1.4) suitably modified by terms allowing for non-uniform area [18–20]. The modified equations can be used for non-spherical tapers, but for the special case of conical tapers, they reduce to the same form as Eqs. (1.1) and (1.2) and, in practice, accurate solutions are possible only with undesirably small grid sizes. Analytical solutions for transient flow in a tapered tube section can be found in [21,22], where the continuous variation of the cross-sectional area leads to continuous reflection of the propagating waves in the positive and negative axial directions.

One purpose of this paper is to present a simple MOC methodology that simulates the behaviour of spherical waves with greater accuracy than is achievable with the use of Eqs. (1.1) and (1.2).

A second purpose is to demonstrate how the method can be coupled to numerical packages based on the use of MOC to predict flows in networks of pipes and ducts. The coupling of one-dimensional methods is far less resource-intensive than fully three-dimensional simulations even though it necessitates the use of smaller time steps of integration than is usual for one-dimensional flows in pipes.

1.2. Outline of paper

The new method is developed in Section 2 and its accuracy is assessed in Sections 3 and 4 by means of two unsteady flows radiating from a sphere. In both cases, the sphere vibrates in a manner that generates a single pulse. The first vibration has a sinusoidal form that is convenient for assessing the general behaviour and the second enables informative comparisons to be made with an analytical solution. This enables the importance of two non-dimensional parameters to be highlighted. One of these is physical (ratio of wavelength : source-radius) and the other is numerical (ratio of wavelength : grid length). The coupling of axial and spherical domains is described in Section 5, which also includes comparisons with predictions using a long-established method of allowing for the consequences of such coupling for wave reflections inside

ducts. Throughout the paper, the mathematical developments are presented in a simple form that is likely to be accessible to engineers wishing to make use of the methodology. This objective is given priority over mathematical conciseness.

For completeness, it is declared that the authors are somewhat surprised that an extensive literature search – together with personal correspondence with a leading world expert on acoustics – has failed to reveal any previous publication of MOC applied to spherical flows in the manner presented herein. Simpler, less accurate, methods exist (see Section 2), but the method presented herein appears to be novel. In a nutshell, the key distinction is the formulation of the equations with rate-of-change-of-flowrate instead of rate-of-change-of-velocity.

2. Spherical MOC

The continuity and momentum equations for spherically symmetric flow may be expressed as

$$\frac{\partial}{\partial t}\left(\rho r^2\right) + \frac{\partial}{\partial r}\left(\rho r^2 u_r\right) = C \tag{2.1}$$

and

$$r^2\frac{\partial}{\partial r}(p) + \frac{\partial}{\partial t}\left(\rho r^2 u_r\right) + \frac{\partial}{\partial r}\left(\rho r^2 {u_r}^2\right) = M \tag{2.2}$$

in which C and M represent external source terms that are included here for generality, but are discarded later in the development. In more general applications than those considered herein, these source terms could represent complications such as body forces or continuous mass loss or addition.

After replacing the second of these equations by a linear combination with the first, we obtain (noting that $\partial r/\partial t = 0$):

$$r^2\frac{\partial}{\partial t}(\rho) + \frac{\partial}{\partial r}\left(\rho r^2 u_r\right) = C \tag{2.3}$$

and

$$r^2\frac{\partial}{\partial r}(p) + \rho\frac{\partial}{\partial t}\left(r^2 u_r\right) + \rho u_r\frac{\partial}{\partial r}\left(r^2 u_r\right) - 2\rho r {u_r}^2 = M - u_r C \tag{2.4}$$

In the following development, the fluid is assumed to be a perfect gas. The corresponding development for a liquid is presented in Appendix A.

For waves that may be assumed to behave isentropically and for a fluid that may be regarded as a perfect gas, the pressure fluctuations will satisfy $p/\rho^\gamma = \text{constant}$. Then, since $c^2 = \mathrm{d}p/\mathrm{d}\rho$, the equations may be written as

$$\frac{2}{\gamma-1}\frac{\partial}{\partial t}(c) + \frac{2}{\gamma-1}u_r\frac{\partial}{\partial r}(c) + \frac{c}{r^2}\frac{\partial}{\partial r}\left(u_r r^2\right) = \frac{c}{\rho r^2}C \tag{2.5}$$

and

$$\frac{2}{\gamma-1}c\frac{\partial}{\partial r}(c) + \frac{1}{r^2}\frac{\partial}{\partial t}\left(r^2 u_r\right) + \frac{u_r}{r^2}\frac{\partial}{\partial r}\left(r^2 u_r\right) = 2\frac{{u_r}^2}{r} + \frac{1}{\rho r^2}(M - u_r C) \tag{2.6}$$

These two equations can be combined into a characteristic form. A simple way to do this is by writing the sum (Eq. (2.5)) ± (Eq. (2.6)), namely

$$\begin{aligned}&\frac{2}{\gamma-1}\frac{\partial}{\partial t}(c) + \frac{2}{\gamma-1}(u_r \pm c)\frac{\partial}{\partial r}(c) \pm \frac{1}{r^2}\frac{\partial}{\partial t}\left(r^2 u_r\right) \pm \frac{1}{r^2}(u_r \pm c)\frac{\partial}{\partial r}\left(r^2 u_r\right)\\ &\quad = \pm 2\frac{{u_r}^2}{r} + \frac{1}{\rho r^2}[\pm M + (c \mp u_r)C]\end{aligned} \tag{2.7}$$

By inspection, the first two terms can be combined as an ordinary differential when $\mathrm{d}r/\mathrm{d}t = u_r \pm c$. So can the second two terms. That is, the pair of equations:

$$\frac{2}{\gamma-1}\frac{d}{dt}(c) \pm \frac{1}{r^2}\frac{d}{dt}\left(r^2 u_r\right) = \pm 2\frac{{u_r}^2}{r} + \frac{1}{\rho r^2}[\pm M + (c \mp u_r)C] \tag{2.8}$$

are valid in the directions

$$\frac{dr}{dt} = u_r \pm c \tag{2.9}$$

If desired, the derivative $\mathrm{d}c/\mathrm{d}t$ in Eqs. (2.8) can be replaced by $(1/\rho c).\mathrm{d}p/\mathrm{d}t$ as, for instance, in Eq. (1.1) above. In this case, however, the coefficient of the derivative is not a formal constant, but instead depends on local flow conditions. That has undesirable consequences for integration when flows have large rates-of-change of pressure.

The coefficient of the second term on the left hand side of Eq. (2.8) highlights the complication that arises from spherical geometry in comparison with uniaxial geometry. It inevitably limits achievable numerical accuracy as r tends to zero, as also do the source terms on the right hand side of the equation. The first of these exists even when there are no source terms in the continuity and momentum equations. The importance of these complications depends strongly on the location in the flow domain. Their influence is dominant at very small radii, but negligible at large radii. Alternative methods of allowing for this are presented in Section 2.2 and the consequential lower limits on the radius at which meaningful predictions can be obtained with plausible grid sizes is explored in Section 3.

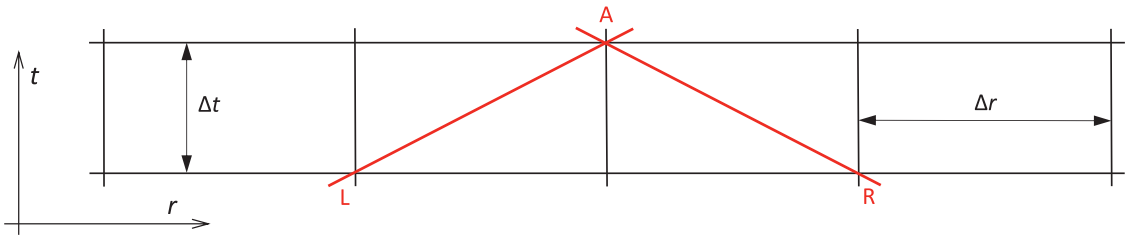

Fig. 1. Characteristic paths in a fixed rectangular r–t grid.

2.1. Flow versus velocity

The numerical integration of Eq. (2.8) is investigated in detail below. However, it is useful to draw attention to some general differences between Eq. (2.8) and Eq. (1.1). The most important of these is the relative balance between the left hand side and right hand side terms. First consider the left hand sides. With Eq. (1.1), the *velocity* has to be integrated directly even though it necessarily tends to infinity as $r \to 0$. In contrast, Eq. (2.8) requires integration of the *flowrate*, which is finite for all radii. Of course, the coefficient $1/r^2$ tends to infinity as $r \to 0$, but this has the effect of a weighting factor that, numerically, can be averaged in various ways over any finite interval with $r > 0$. Thus the left hand side of Eq. (2.8) is more benign (numerically) than that of Eq. (1.1). A further practical benefit of Eq. (2.8) is that its left hand side embraces the character of the flow behaviour more fully than that of Eq. (1.1). As a consequence, the source terms on the right hand side of Eq. (2.8) have a smaller influence on the integration than those of Eq. (1.1), thereby enabling the use of larger time steps for integration.

2.2. Numerical integration

The characteristic equations are valid at all $r > 0$ and at all times. They permit consideration of the external source terms C and M and they are not restricted to small amplitude fluctuations. For the special purposes of this paper, however, attention is focused on cases for which $C = 0$ and $M = 0$ and, in this case, the second term on the right-hand side of Eq. (2.8) vanishes. In a typical numerical simulation, the equations are integrated in a time-marching manner to yield values of the flow parameters at a typical point A at the intersection of two characteristics on which solutions have been obtained at earlier instants as illustrated in Fig. 1. The first term in Eq. (2.8) can be integrated exactly, but the other two terms require approximations. Herein, the chosen approximate integrations are, along LA, for example:

$$\int_L^A \frac{2}{\gamma - 1}\frac{d}{dt}(c)dt = \frac{2}{\gamma - 1}(c_A - c_L) \tag{2.10}$$

$$\int_L^A \frac{1}{r^2}\frac{d}{dt}\left(r^2 u_r\right)dt \cong \overline{\left(\frac{1}{r^2}\right)}_{LA}\left[\left(r^2 u_r\right)_A - \left(r^2 u_r\right)_L\right] = \left(\frac{r_A u_{rA}}{r_L} - \frac{r_L u_{rL}}{r_A}\right) \tag{2.11}$$

$$\int_L^A 2\frac{{u_r}^2}{r}dt \cong \left(\frac{{u_{rA}}^2}{r_A} + \frac{{u_{rL}}^2}{r_L}\right)\Delta t \tag{2.12}$$

In the development of Eq. (2.11), the average value of $1/r^2$ along LA is taken as $1/(r_L r_A)$, which would be exactly correct if r varied linearly in time along the characteristic line (as in Fig. 1). This implies that the gradient of the characteristic line is assumed to be approximately constant and this, in turn, limits the range of applicability of the solution to small Mach numbers. Even with this assumption, however, the integration of the whole term involves approximation because the coefficient $(1/r^2)_{\mathrm{LA}}$ is treated as a constant. An alternative to Eq. (2.11) can be obtained as follows:

$$\begin{aligned}\int_L^A \frac{1}{r^2}\frac{d}{dt}\left(r^2 u_r\right)dt &= \int_L^A \frac{du_r}{dt} + \frac{2u_r}{r}\frac{dr}{dt}dt = \int_L^A \frac{du_r}{dt}dt + 2\int_L^A u_r\frac{d\ln r}{dt}dt \\ &\cong [u_r]_L^A + 2\overline{u_r}[\ln r]_L^A = (u_{rA} - u_{rL}) + (u_{rA} + u_{rL})\ln\frac{r_A}{r_L}\end{aligned} \tag{2.13}$$

Note that the velocity tends to infinity as the radius tends to zero. A detailed comparison of the two approximations (2.11) and (2.13) by using a spreadsheet has shown that, numerically, the difference between them varies closely with $[(\Delta r)/r]^2$, being approximately 1% when $(\Delta r)/r = 0.25$.

Similar issues arise with the integration of the term ${u_r}^2/r$ in Eq. (2.8). Indeed, this is even more sensitive to the Mach number and to small values of r. In a *steady* spherical flow, this term would be proportional to $1/r^3$ and so an accurate integration could be obtained between any two finite radii. In a wave-like flow, however, it is not safe to assume that the velocity will vary inversely with radius (or even that it decreases with increasing radius). For the simulations presented

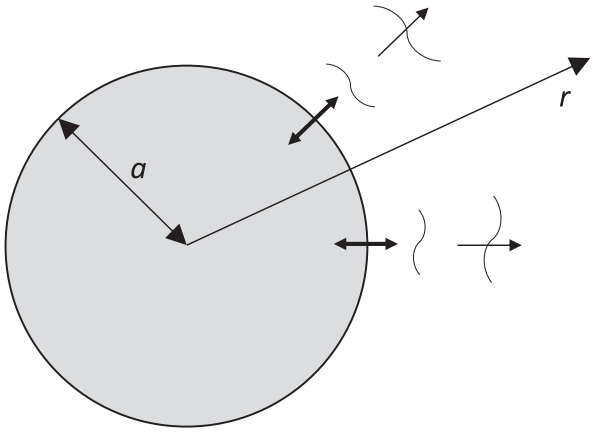

Fig. 2. Waves radiating from a pulsating sphere.

herein, the integration is approximated as shown in Eq. (2.12). The consequences of this approximation – together with that of the other right-hand-side term in Eq. (2.8) – are assessed in Section 3.

Eqs. (2.10)–(2.12), together with corresponding approximations along LR, yield a pair of simultaneous equations in c_A and u_{rA} that can be expressed as

$$\frac{2}{\gamma-1}c_A+\left(\frac{r_A}{r_L}-\frac{u_{rA}}{r_A}\Delta t\right)u_{rA}=\frac{2}{\gamma-1}c_L+\left(\frac{r_L}{r_A}-\frac{u_{rL}}{r_L}\Delta t\right)u_{rL} \tag{2.14}$$

and

$$\frac{2}{\gamma-1}c_A-\left(\frac{r_A}{r_R}-\frac{u_{rA}}{r_A}\Delta t\right)u_{rA}=\frac{2}{\gamma-1}c_R-\left(\frac{r_R}{r_A}-\frac{u_{rR}}{r_L}\Delta t\right)u_{rR} \tag{2.15}$$

in which the left-hand sides depend on the unknown parameters c_A, u_{rA} and the right-hand sides depend solely on coordinates and parameters with known values.

Subtraction of one of these equations from the other yields a quadratic equation that can be solved for u_{rA} and back-substitution then yields c_A. Alternatively, the solution can be obtained iteratively, treating Eqs. (2.14) and (2.15) as a pair of linear simultaneous equations in which the coefficients of u_{rA} are updated continuously until convergence is achieved. The latter approach is especially convenient at large radii because the quadratic term is very small and so convergence is achieved rapidly.

2.3. Boundary conditions

Boundary conditions are required at the inner and outer radii of the flow domain. Herein, as in most practical simulations, disturbances propagate radially outwards from the driving boundary at the inner radius. The particular condition is case-specific, being wholly dependent on the physical phenomenon under investigation. In contrast, the outer boundary condition will not normally be case-specific. Usually, as herein, it will be treated in a manner that serves the same generic purpose as a null-reflection boundary condition in a uniaxial flow. In the spherical case, however, the description 'null-reflection' would be inappropriate because no such condition is possible in a spherically symmetric flow. In analytical solutions, the outer boundary can be chosen at infinity, but this is not possible in numerical solutions. However, the boundary can usually be chosen at a radius that is sufficiently large for acoustic, far-field conditions to be assumed. That is, it is assumed that the product rp' is constant in a characteristic direction satisfying $\mathrm{d}r/\mathrm{d}t=c_0$, where $p'=p-p_0$ and the suffix 0 denotes the initial undisturbed conditions (see Appendix B).

3. Pulsating sphere – sine wave excitation

The use of the analysis is now illustrated for the particular case of waves propagating radially outwards in an infinite flow-field outside a pulsing sphere of radius $r=a$ (Fig. 2). This simple case is instructive because comparisons can be made with an analytical solution (derived in Appendix B), thereby enabling the limitations of the methodology to be explored. In this Section 3, all results are numerical and the emphasis is on physical behaviour and on investigating what grid size is necessary to achieve numerical convergence. Then, in Section 4, direct comparisons between numerical and analytical predictions are presented to verify that the converged solutions are valid.

As usual in numerical integrations, it is important to ensure that integration steps are sufficiently small to avoid the growth of unacceptably large numerical errors. In this instance, there are two key sources of such error. First, for any particular grid length Δr, numerical approximations of ratios such as r_A/r_L and u_{rA}/r_A in Eqs. (2.14) and (2.15) are inevitably

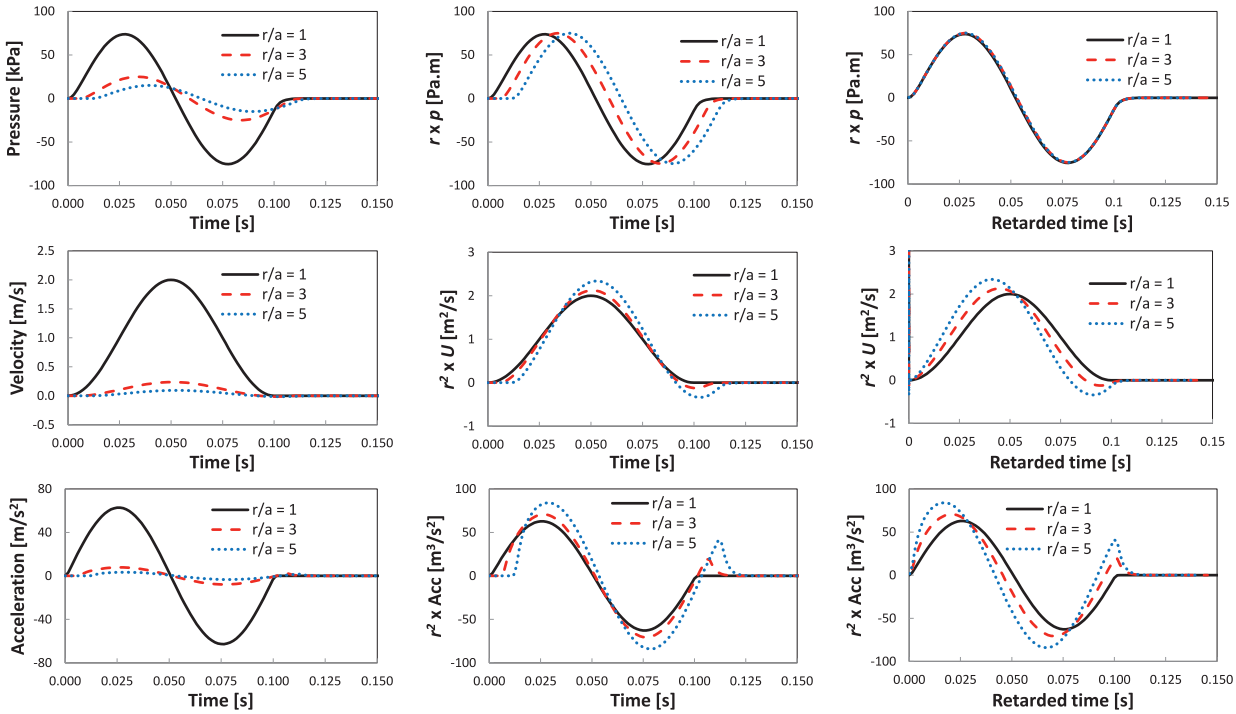

Fig. 3. Pressure, velocity and acceleration for a sine wave pulse with a period of 100 ms.

less reasonable at small radii than at large radii. To allow for this, it is necessary to use grid lengths that ensure sufficiently small values of the ratio $(r_A - r_L)/[½(r_A + r_L)]$ even at the smallest radius in the computational domain. This is a much more demanding constraint than in the corresponding case of steady flows because variable grid sizes are not practicable. It is desirable to use a common time step over the whole of the computational domain and, for explicit schemes, this implies using a common spatial step too. Both the spatial grid size and the integration time step are determined by the most demanding location, namely at the smallest radius in the domain, and the required computational resource therefore increases with $1/(\Delta r)^2$. This is especially wasteful in domains where the ratio of the outer and inner radii is large.

In practice, this numerical limitation on acceptable grid sizes is not always the critical factor. In addition to needing to obtain valid solutions of the governing equations, it is necessary to ensure that outcomes are expressed in sufficient detail for practical purposes. For a vibrating sphere, for instance, the numerical discretisation must be sufficiently detailed to represent the highest frequencies of practical interest. If this condition is not met, peak amplitudes can be missed and, in extreme cases, aliasing effects can lead to grossly misleading interpretations of predictions. Strictly, this is not a numerical error per se; it is a consequence of inappropriate discretisation of boundary conditions and/or numerical output. Nevertheless, this requirement can be more demanding than that of achieving formal numerical accuracy – e.g. when high-frequency disturbances propagate from a large-diameter source.

The second of these requirements is addressed in Section 3.1, thereby enabling Section 3.2 to focus exclusively on the numerical grid size needed to ensure adequate convergence. Then, in Section 4, numerical solutions are compared with analytical predictions to assess the validity of the numerical convergence.

3.1. Influence of λ/a

Fig. 3 shows predicted pressure variations outside a sphere of radius $a = 1$ m when the prescribed velocity at the surface of the sphere varies as one cycle of a sine wave with an amplitude of 1 m/s and a time period of 100 ms. The datum is offset by 1 m/s so that the accelerations at the beginning and end of the period are zero. The fluid is assumed to be a perfect gas for which the specific gas constant is $R_{gas} = 287$ J/kg K and the ratio of the principal specific heats is $\gamma = 1.401$. These values are indicative of dry air. The initial pressure and temperature are chosen as $p_0 = 100$ kPa and $T_0 = 15$ °C (= 288.15 K) respectively. The implied initial density is $\rho_0 = p_0/RT_0 = 1.209$ kg/m^3 and the isentropic speed of sound is $c_0 = (\gamma RT_0)^{½} = 340.4$ m/s, implying a wavelength of $\lambda = c_0/f = 34.04$ m. The latter values are shown in the first block of Table 1 together with the corresponding values of the key ratios $\Delta r/a$ and $\Delta r/\lambda$.

The left-most column in Fig. 3 shows predicted values of the (gauge) pressure, velocity and acceleration at $r/a = 1$, 3 and 5. The pressures and velocities are obtained directly from the numerical solution, but the accelerations have been derived from numerical differentiation of the velocity history and are therefore of lower accuracy. This will rarely be important in

Table 1
Non-dimensional ratios $\Delta r/\lambda$, $\Delta r/a$ and λ/a.

τ [s]	λ [m]	Δr [m]	$\Delta r/\lambda$	$\Delta r/a$	λ/a
10^{-1}	34.04	1.00	0.0294	1.00	34.04
		2.00	0.0588	2.00	34.04
		4.00	0.1175	4.00	34.04
10^{-2}	3.404	0.10	0.0294	0.10	3.404
		0.20	0.0588	0.20	3.404
		0.40	0.1175	0.40	3.404
10^{-3}	0.3404	0.01	0.0294	0.01	0.3404
		0.02	0.0588	0.02	0.3404
		0.04	0.1175	0.04	0.3404

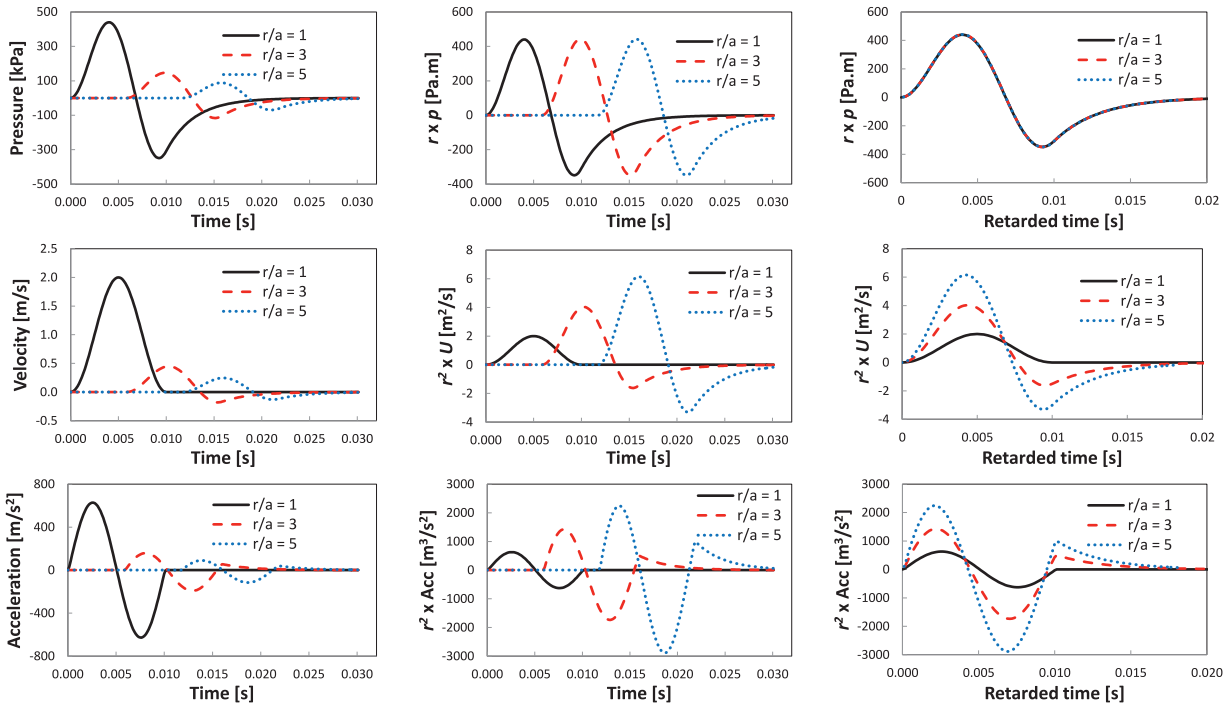

Fig. 4. Pressure, velocity and acceleration for a sine wave pulse with a period of 10 ms.

practical applications because the acceleration history is not usually of interest in its own right. For the purposes of this particular paper, however, it is useful because it helps to illustrate the physical behaviour. For example, Fig. 3 shows that, at the surface of the sphere ($r/a = 1$), the pressure variation is almost in phase with the acceleration. This correlation is less strong at larger radii (e.g. $r/a = 5$), but it is closer than the correlation between pressure and velocity. Behaviour such as this is characteristic of the near-field behaviour of a monopole [23,24]. Different behaviour is illustrated in later examples.

The central column of Fig. 3 shows the same data in a scaled form and the right-most column shows the scaled data offset by the time required for sound waves to travel from the sphere surface (i.e. so-called retarded time). By inspection, as required analytically, the variation in the product $r.p'$ is effectively independent of radius, thereby giving confidence in the accuracy of the numerical implementation. This is assessed more rigorously below. In contrast with the pressure, the velocity and acceleration are scaled by r^2, giving behaviour that corresponds to the volumetric flowrate and its rate of change. These increase slightly with increasing distance, but at much smaller rates than the decrease of absolute velocity and acceleration (left-most column).

The particular outcome presented in Fig. 3 is specific to the chosen wavelength λ. This can be seen from Fig. 4 which shows the corresponding outcome with a wavelength that is 10 times smaller, i.e. $\lambda\ /a = 3.404$ m. The predicted behaviour at the surface of the sphere is broadly similar to that with the longer wavelength, but the behaviour at greater radii is significantly different. First, the amplitudes of velocity and acceleration do not decay so rapidly and so the scaled values increase strongly with increasing distance from the sphere. Second, at the larger values of r/a, the qualitative behaviour of the pressure correlates much more closely with the velocity than with the acceleration. This behaviour is broadly characteristic of the far-field behaviour of a monopole.

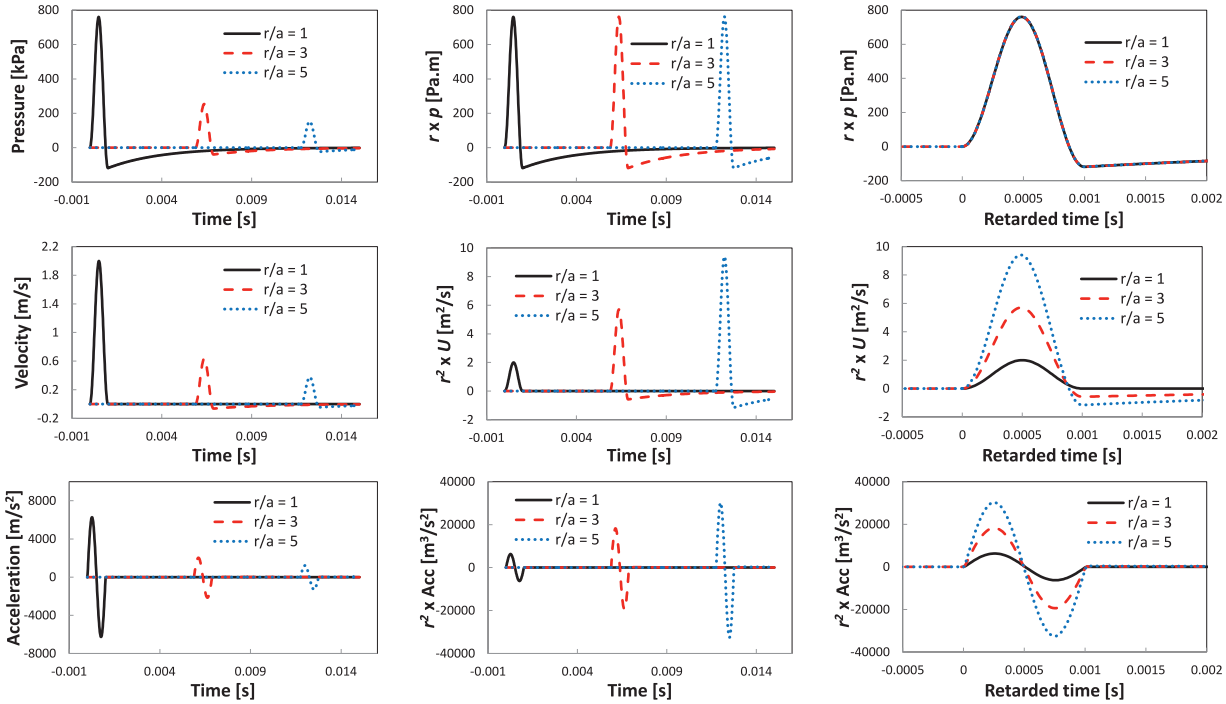

Fig. 5. Pressure, velocity and acceleration for a sine wave pulse with a period of 1 ms.

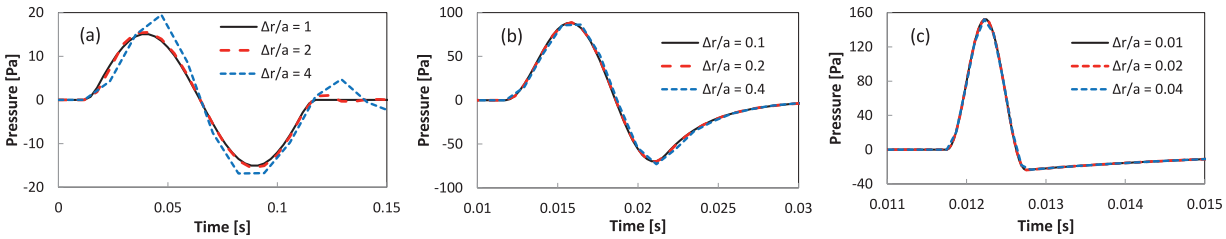

Fig. 6. Influence of grid size: pressures at $r/a = 5$.

Fig. 5 shows the corresponding predictions with a wavelength that is shorter by a further factor of 10, i.e. $\lambda\ /a = 0.3404$ m. In this case, the far-field behaviour extends down to much smaller radii, almost as far as the surface of the sphere itself. The velocities at each of the outer radii shown (i.e. $r/a = 3$ and 5) scale closely with $1/r$, not with $1/r^2$ as in Fig. 3. This similarity with the exact scaling of pressure with $1/r$ is consistent with the asymptotic condition known analytically, namely that the *local* wave behaviour at large radii is almost identical to that of linear one-dimensional wave propagation [23].

3.2. Influence of $\Delta r/\lambda$ and $\Delta r/a$

In Section 3.1, the primary focus is on physical behaviour. Attention now turns to the influence of the numerical grid size. Fig. 6 shows the predicted pressure history at $r = 5a$ for each of the cases discussed so far, namely $\tau = 100$, 10 and 1 ms and, in each case, predictions are shown for three values of the grid length Δr. The implied values of the ratios $\Delta r/\lambda$, $\Delta r/a$ and λ/a are listed in Table 1. The same three values of $\Delta r/\lambda$ are used in all three cases and, as a consequence, the ratio $\Delta r/a$ is scaled with the wavelength. For the case $\tau = 100$ ms, the smallest grid length considered is equal to the radius of the sphere ($a = 1$ m). For the other two cases, all three grid lengths are smaller than the sphere radius.

One obvious trend highlighted by Fig. 6 is a reducing accuracy of the numerical predictions with increasing $\Delta r/\lambda$ at constant $\Delta r/a$. This is primarily a consequence of a coarse discretisation of the prescribed wave at the inner boundary condition. With the finest grid lengths, the wave is represented by approximately 34 intervals whereas, with the coarsest grid lengths, it is represented by only a quarter of this number so each interval is quite large. Even in this case, the calculated values of pressure and velocity are close to the correct values, but the inferred accelerations (not shown) are poor because strong changes occur in the intervals over which they are deduced from the predicted velocities.

A less obvious trend revealed in Fig. 6 is the reducing accuracy of the numerical predictions with increasing $\Delta r/a$ at constant $\Delta r/\lambda$. This is primarily a consequence of the influence of ratios such as r_A/r_L and u_{rA}/r_A in the MOC equations. Its

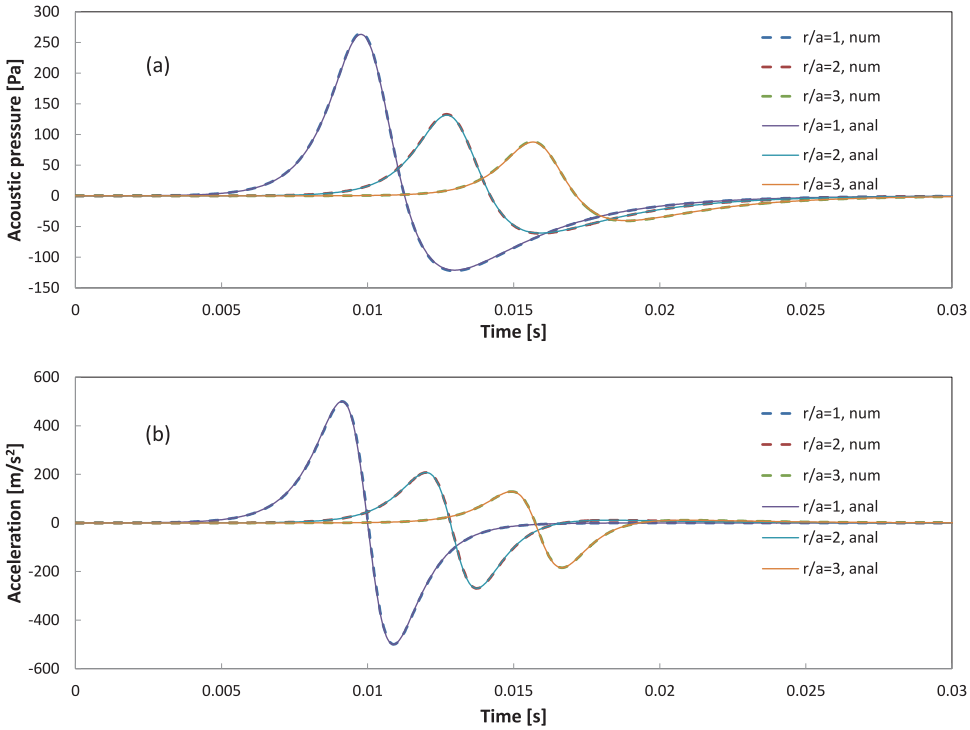

Fig. 7. Pressure and acceleration for a sech wave pulse ($\tau = 10$ ms).

effect is masked when $\lambda < a$ because the need to have small $\Delta r/\lambda$ automatically ensures that $\Delta r/a$ is also small. For larger wavelengths, however, it becomes the dominant factor constraining the acceptable grid size. In effect, it limits the lower bound of inner radii that can be considered in practical numerical simulations.

For completeness, note that the grid sizes used for the simulations reported in Figs. 3–5 were half of the smallest values listed in Table 1. It can be inferred from Fig. 6 that this ensures adequate numerical convergence, as is essential for the purposes of those figures, namely assessing the influence of λ/a.

4. Pulsating sphere – sech wave excitation

Although the above results demonstrate that the numerical solution converges as the grid size is reduced, they do not explicitly demonstrate that the converged result is valid. For this purpose, it is necessary to make comparisons with a case for which analytical predictions are possible. In principle, the most obvious possibility would be to choose the harmonic case of a *continuous* sine wave. However, this option has an inherent disadvantage because the numerical solution necessarily starts from a prescribed initial condition and several cycles must elapse before meaningful comparisons can be made with analytical predictions of the asymptotic condition. Furthermore, small differences between similar waves of identical frequency can be difficult to observe. Instead, the chosen case is a single velocity pulse defined by:

$$U_{r=a} = U_o \mathrm{sech}\left\{\beta\left(\frac{t}{\tau} - 1\right)\right\} \tag{4.1}$$

in which U_0 is the maximum amplitude of the velocity at the surface of the sphere, τ is the pulse duration and $\beta = 10$ is a simple scaling-and-shifting factor. An analytical solution for this case is presented in Appendix B.2

Figs. 7 and 8 show analytical and numerical predictions for pulses of 10 ms and 1 ms duration, respectively. In both cases, the inner boundary condition is the prescribed velocity at the surface of the sphere. This defines the accelerations shown in the figures at $r/a = 1$, but all other curves in the figures are predicted outcomes. By inspection, the predicted pressure and velocity histories coincide almost exactly with the analytical solution so it may be concluded that the converged analysis does indeed yield valid solutions. Furthermore, the predicted accelerations also coincide almost exactly with the analytical solution. This is an even stronger confirmation of the validity because, as indicated above, the MOC predictions of accelerations have been obtained by numerical differentiation of a set of discrete velocity-time points.

5. Radiation from a duct exit

The case considered so far has the special advantage of being well-understood and amenable to analytical analysis. This has enabled the strengths and limitations of the spherical MOC method to be assessed in a rigorous manner. However,

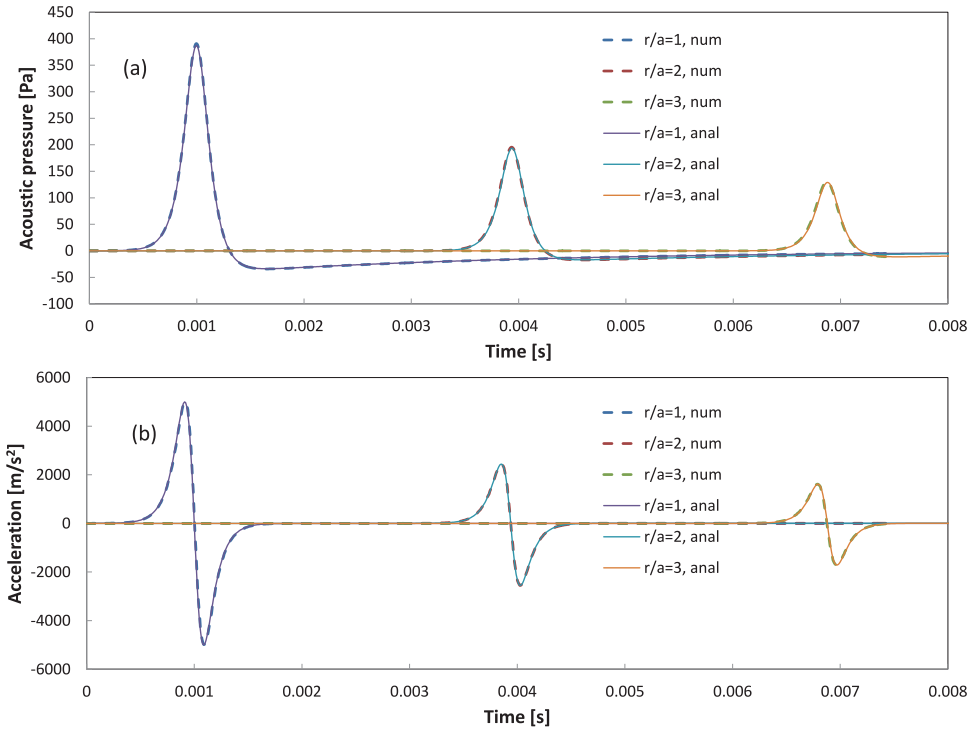

Fig. 8. Pressure and acceleration for a sech wave pulse ($\tau = 1$ ms).

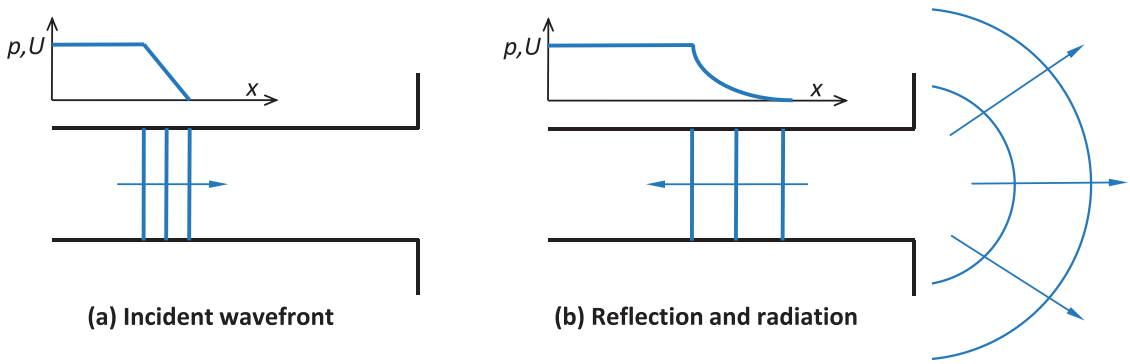

Fig. 9. Reflection and radiation of a wavefront at a duct exit.

practical applications are less simple. The inner boundary is unlikely to be perfectly spherical; the prescribed condition at the boundary is unlikely to be a known variation of velocity; the excitation is unlikely to be a single frequency or a single pulse. In the following example, featuring pressures (e.g. sound) radiated from a duct exit, none of these conditions prevails.

Fig. 9 depicts a wavefront propagating along a duct towards a flanged exit, at which it partially reflects and partially radiates into the external environment. The particular wavefront shown corresponds to a linear rate of change, thereby enabling the qualitative consequences for the reflected wave to be visualised easily. The details depend upon the particular shape, but the overall behaviour will occur for any wavefront. Sufficiently far from the exit plane, the reflected wavefront must satisfy the dynamics of ducted flows and the external radiation must satisfy the dynamics of spherical flows. In a transitional zone close to the portal, however, neither of these asymptotic conditions will prevail. Instead, in each region, the behaviour will be influenced by the requirements of the other region. In the following development, the transitional zone is compressed into a discrete interface at which uniaxial one-dimensional behaviour changes abruptly to spherically one-dimensional behaviour (Fig. 10). This idealisation is implemented in a manner that, for isentropic flows, respects conservation of mass and energy. Furthermore, the radius of the 'inner' boundary of the external hemispherical domain is chosen so that its surface area is equal to the cross-sectional area of the duct, i.e. $a = R\sqrt{2}$, thereby achieving continuity of velocity (assuming negligible change in density at the interface).

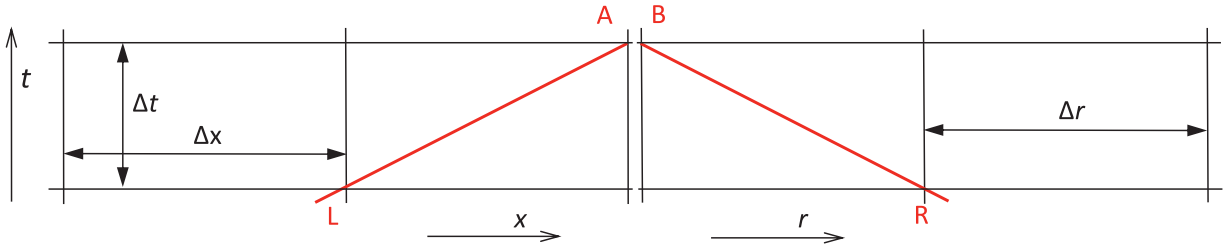

Fig. 10. Interface between uniaxial and spherical characteristic grids.

Naturally, the use of an interface that is itself a geometrical discontinuity negates the possibility of obtaining solutions that are exact in a formal mathematical sense. However, it is also true that no one-dimensional analysis can simulate three-dimensional phenomena correctly. What matters is whether they can do so with sufficient accuracy for the purposes for which they are undertaken. In the present case, the fundamental objective is to achieve a step improvement on established methods that are of lower accuracy. In particular, it is desired to assess – and improve upon – methods that link uniaxial and spherical wave propagation in uncoupled manners.

In the *steady* flow of a real fluid from a duct, outflows occur in the form of a jet that differs hugely from the spherical acoustical behaviour shown in Fig. 9. However, this is not important for present purposes because, for low Mach numbers, the development time for such flows greatly exceeds the short timescales relevant to the early stages of wavefront reflections. Indeed, even if a steady flow with a well-established jet existed already, it would have little influence on the reflection process. In effect, the wavefront behaviour would initially superimpose on the pre-existing steady flow, evolving only slowly to a new steady flow at increased velocity. Nevertheless, the assumption of spherically-symmetric flow is an imperfect representation of the true wave behaviour, which does exhibit a directional dependence [4]. The true flow field has some characteristics of a doublet, with radiation in the direction of the duct axis being stronger than that normal to the axis.

Using the notation in Fig. 10, the linear and spherical MOC equations on the two sides of the interface are

$$\frac{2}{\gamma-1}c_A + u_{xA} = \frac{2}{\gamma-1}c_L + u_{xL} \tag{5.1}$$

and

$$\frac{2}{\gamma-1}c_B - \left(\frac{r_B}{r_R} - \frac{u_{rB}}{r_B}\Delta t\right)u_{rB} = \frac{2}{\gamma-1}c_R - \left(\frac{r_R}{r_B} - \frac{u_{rR}}{r_L}\Delta t\right)u_{rR} \tag{5.2}$$

respectively, and these become a pair of linear simultaneous equations in c and u when continuity of sound speed and particle speed is imposed, namely

$$c_A = c_B \tag{5.3}$$

and

$$u_{xA} = u_{rB} \tag{5.4}$$

5.1. Reflected wavefront inside the duct

Fig. 11 shows predicted pressure histories inside a duct shortly after an incident wavefront reflects at the flanged end of the duct. The wavefront is generated by prescribing the pressure history at an upstream boundary in the form of an arctan. For a time axis t^* chosen relative to the mid-point of the wavefront, the relationship is

$$\frac{p'}{p'_\infty} = \frac{1}{2} + \frac{1}{\pi}\arctan\left[\frac{Act^*}{R}\right] \tag{5.5}$$

where p'_∞ is the overall amplitude of the wavefront, R denotes the duct radius ($\sqrt{2}$ m), c is the speed of sound (340.4 m/s in the ambient air) and A is a coefficient chosen to achieve the desired rate of change of pressure – which is a maximum at $t^* = 0$. Close to the leading and trailing edges of the wavefront, the asymptotic behaviour of the arctan is replaced by a simple quadratic form, thereby avoiding the existence of discontinuous gradients at the extremes. The graphs are shown during a period after the incident wavefront has passed and at a location inside the duct that is 50 m from the exit. For the simulations presented herein, this is sufficiently far from the exit to avoid any overlapping of the incident wavefront and its reflection.

At any particular location, the incident wavefront causes the pressure to rise monotonically to 1 kPa and this value is sustained until the reflected wavefront begins to arrive (at about $t = 0.89$ s in Fig. 11). The incident wavefront causes the velocity to increase from zero to approximately 2.5 m/s. Three reflected curves are shown. One (uncoupled) shows predictions

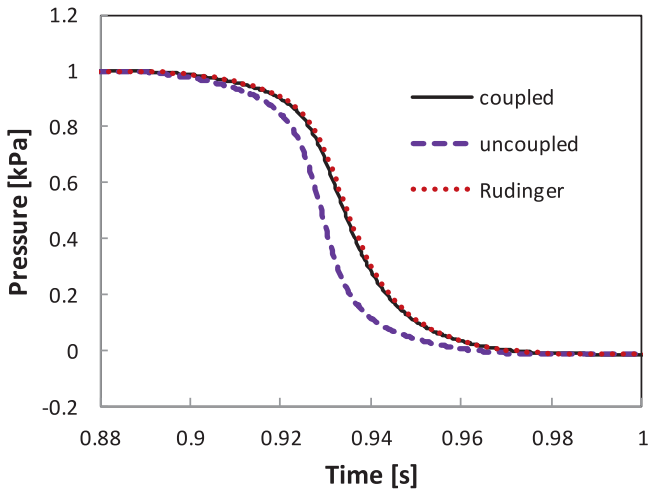

Fig. 11. Wavefront reflected inside duct (intitial $(\partial p/\partial t)_{\max} = 50\,\text{kPa/s}$).

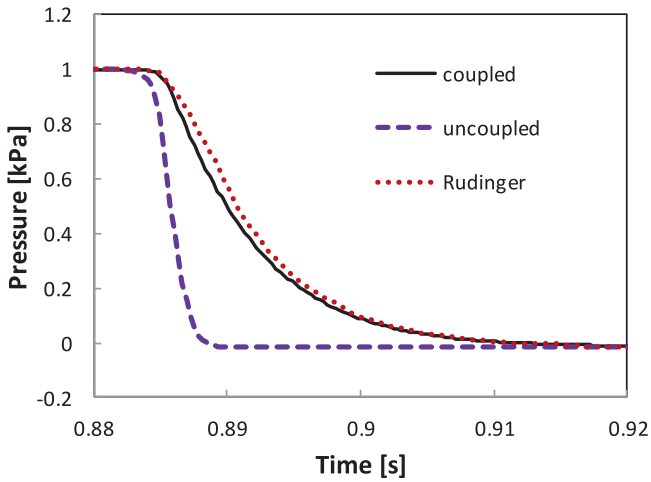

Fig. 12. Wavefront reflected inside duct (intitial $(\partial p/\partial t)_{\max} = 500\,\text{kPa/s}$).

based on an assumed constant pressure at the exit plane throughout the reflection process. For this case, which is commonly used in simulations of unsteady flows in ducts, the shape of the reflected wavefront is almost identical to the shape of the original incident wavefront. The other two (coupled and Rudinger) show predictions that allow for delays caused by interaction during the reflection process. These are sufficiently similar to each other to be only just distinguishable in the figure, but both differ markedly from the first case. One shows predictions based on the coupled MOC analysis presented above and the other shows predictions using an analysis presented by Rudinger [25] that allows for the influence of the external flow field, but does not include predictions within that flow field. For completeness, note that although Rudinger's method has been implemented in the manner he presented, the numerical values in his paper have been updated using higher precision and smaller time intervals – see Brown and Vardy [26].

For completeness, it is pointed out that the incident wavefront shortens (steepens) slightly as it approaches the duct exit and lengthens again as it reflects back upstream. The software allows for this behaviour within the duct even though its influence on the predicted pressures is negligible for present purposes. As can be seen in the above equations, no such allowance is made for such non-linear behaviour outside the duct, but the effect is much smaller there because the velocities are smaller.

Fig. 12 shows the corresponding predictions for an incident wavefront with the same shape except that the timescale is ten times smaller. With this higher-frequency case, the influence of the delay is much stronger than in Fig. 11 even though the absolute delay is similar in both cases. In addition, there are now clearly detectable differences between the predictions of the present analysis and those based on Rudinger's method. Unfortunately, the authors are unable to apportion these differences reliably. In effect, both methods treat the incident wavefront as a series of small waves, each of which can be regarded either as continuous (MOC) or as a weak shock (Rudinger). Also, both methods assume plane-wave behaviour

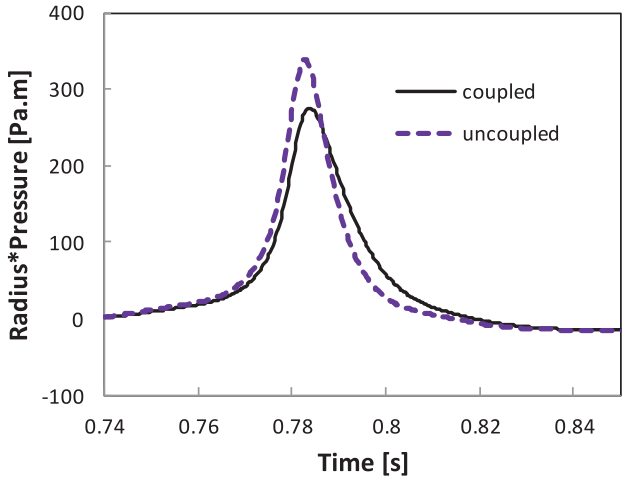

Fig. 13. Radiation from duct exit (intitial $(\partial p/\partial t)_{\max} = 50$ kPa/s).

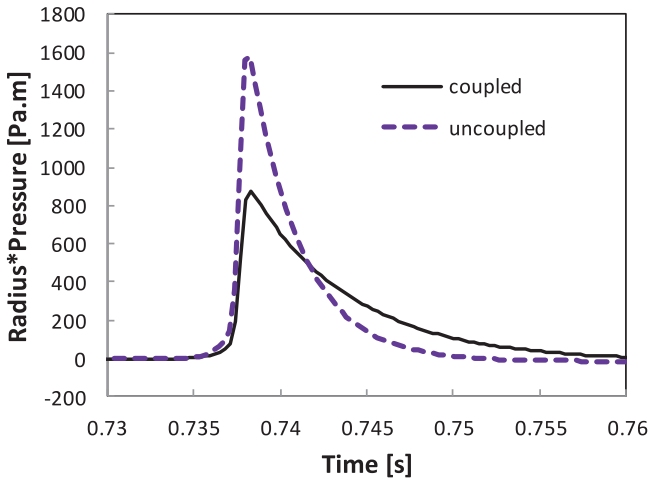

Fig. 14. Radiation from duct exit (intitial $(\partial p/\partial t)_{\max} = 500$ kPa/s).

inside the duct, even close to the exit plane. The present analysis then has a geometrical discontinuity with an instantaneous change from uniaxial to spherical geometry. In each domain, numerical errors are small (assuming sufficiently small grid sizes) but the discontinuous geometry fundamentally limits the accuracy of the overall solution. Rudinger's method has no geometrical discontinuity, but its accuracy will be limited by whatever method was chosen to sum radiation from each part of the exit plane. Physically, radiation from the circumference of the duct commences before radiation from regions at smaller radii. It is not clear whether or how Rudinger's frequency-dependent acoustic impedance allows for this effect.

5.2. Radiated waves outside the duct

Figs. 13 and 14 show pressures predicted at the inner boundary ($r = a$) using the spherical analysis for the same cases as those shown in Figs. 11 and 12. The continuous lines show predictions obtained using the coupled method and the broken lines show predictions based on the decoupled, two-step method. In the latter case, the uniaxial solution is used to predict the velocity – and hence the volumetric flowrate – at the exit plane, based on the assumption of constant pressure at that location. This flowrate history is then used as the inner boundary condition for the spherical domain.

By inspection, the decoupled method overestimates the true pressures and underestimates the decay time. The overestimation of pressure is easily understood. The assumption of unchanging pressure at the exit plane in the uniaxial simulation causes an overestimation of the velocity during the reflection of the incident wavefront. This overestimation is conveyed directly to the spherical analysis as its inner boundary condition. The importance of this effect depends upon the relative time scales of (i) the incident wavefront and (ii) wave propagation through the near-field region of the spherical domain. It is much stronger in the higher-frequency case than in the lower-frequency case.

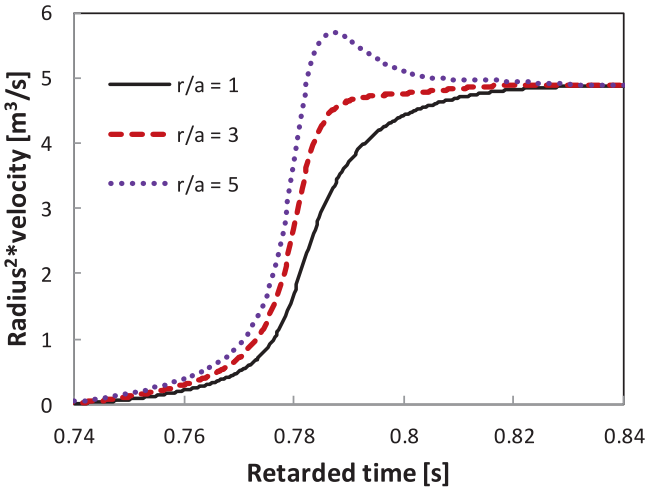

Fig. 15. Radiated wave (intitial $(\partial p/\partial t)_{\max} = 50$ kPa/s).

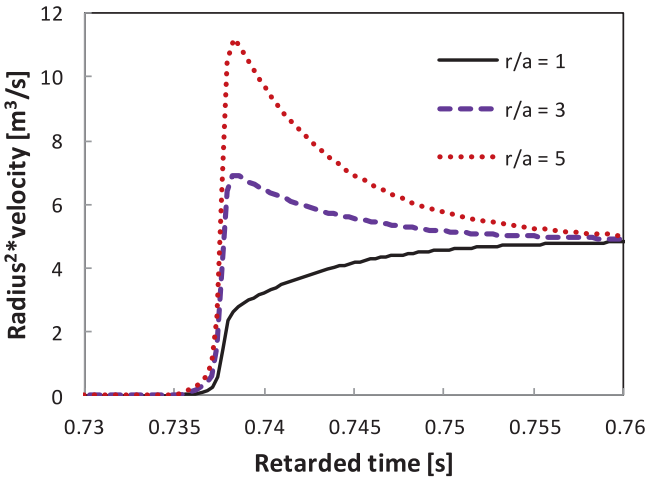

Fig. 16. Radiated wave (intitial $(\partial p/\partial t)_{\max} = 500$ kPa/s).

Although Figs. 13 and 14 highlight errors resulting from the use of the decoupled methodology, they can also be used to justify its use in practical applications where the ratio of the above time scales is sufficiently large. The big discontinuity in pressure at the boundaries of the two decoupled domains ($p' = 0$ at the exit plane in the uniaxial simulation) causes only a moderate error in the inferred flowrate and hence in the predicted external pressures.

Another important feature of Figs. 13 and 14 is the inverse relationship between the maximum pressure and the wavefront duration. This is easily explained by considering a simple monopole. The maximum pressure at any location in the spherical flow field around a monopole is proportional to the maximum rate of change of flowrate assumed at the origin. For the decoupled case, the predicted rates of change of flowrate at the exit plane are inversely proportional to the duration of the incident wavefront. Accordingly, if the predicted (decoupled) flowrate were assumed at the origin of a monopole, the maximum pressure in the external flow-field would be inversely proportional to the duration of the incident wavefront. In the above simulations, the inferred velocity is imposed at a finite radius, not at the origin, so the resulting pressures differ from those in a monopole. Nevertheless, the underlying effects are similar.

5.2.1. Far field

Figs. 13 and 14 are directly applicable at the inner boundary of the spherical domain ($r = a$), but they are also valid for all radii $r > a$. However, they provide little information about the relative importance of near-field and far-field behaviour in the spherical domain. For this purpose, it is necessary to inspect flow histories at two or more locations.

Figs. 15 and 16 show flow histories at $r/a = 1$, 3 and 5. In both simulations, the product $r^2 u_r$ becomes asymptotic to a common value as time increases. This is a simple consequence of the existence of a uniform flowrate from the duct after the reflection of the wavefront has occurred. In the higher-frequency case (Fig. 16), the shape of the predicted velocity history at $r/a = 5$ closely resembles that of the pressure history, thereby showing that the conditions at this radius correspond

approximately to far-field behaviour. The similarity is much less strong at $r/a = 3$ and it is almost totally absent at $r/a = 1$. At the inner locations, the velocity lags the pressure strongly because the small time scales imply relatively large accelerations. In effect, the acceleration acts as a strong damper on the velocity response.

The influence of accelerations is much less strong in the lower-frequency case (Fig. 15) because, for any particular velocity change, the greater timescales imply smaller accelerations. Nevertheless, the velocity clearly lags the pressure during the initial rise and this behaviour also exists at the larger radii. For example, the maximum velocity at $r/a = 5$ occurs at approximately 0.787 s whereas the maximum pressure occurs at approximately 0.784 s. At the smaller radii, the velocity does not reach a peak, but instead approaches its limiting value asymptotically. This is loosely indicative of near-field behaviour.

6. Other methods of solution

The methodology presented above is simple and it reproduces the behaviour of both near-field and far-field variations in pressure and velocity. It has the advantage of being able to accommodate almost any continuous incident wavefront in the uniaxial domain and it could be implemented at multiple exits of a network of ducts. It is hugely less resource-intensive than fully three-dimensional methods, regardless of whether these are implemented in a coupled or decoupled manner or, indeed are used to simulate the whole network.

Notwithstanding this advantage, the need for an abrupt interface between linear and spherical coordinates at the duct exit inevitably introduces errors so it is appropriate to consider the possibility of an intermediate case between fully 1-D and fully 3-D. One such method, proposed by Kirchhoff and based on Huygen's principle [27], attempts to allow for the finite size of the exit plane. In this methodology, the internal and external solutions are decoupled. First, the internal flows are simulated using 1-D analyses and are used to predict mass flowrates at the exit portal. Then these mass flowrates are used as input to the external flow-field. For this purpose, the exit plane is discretised as many small planes, each causing radiation into the external domain. The overall solution in the external domain is then regarded as a combination of multiple monopoles with origins at the centroids of the discrete elements.

At first sight, this is an attractive approach, especially for predictions close to the exit plane where the assumption of overall spherical behaviour is least reasonable. Nevertheless, it has two drawbacks in addition to requiring more complex coding than the method introduced herein. First, in common with the decoupled methodology discussed above, the inferred flowrate through the exit plane takes no account of the influence of the external flow-field on the reflection/radiation process. Second, in the absence of knowledge of the true distribution of the flowrate over the exit plane, it is necessary to estimate the flowrates through individual elements of the plane in an essentially arbitrary manner, typically assuming uniform velocity over the whole plane. As a consequence, although this approach is likely to be more accurate than specifying a single monopole at the centroid of the exit plane, it is not necessarily more accurate than the decoupled method described above, in which the inner boundary of the spherical analysis is a *finite* spherical surface. It is even less certain that it will be better than the coupled approach that overcomes the deficiency highlighted in Figs. 13 and 14.

7. Conclusions

A one-dimensional method of characteristics has been developed for the simulation of spherically symmetric unsteady flows and has been validated by comparison with an analytical solution for a discrete pulse initiated at the surface of a vibrating sphere. The method has been coupled to a one-dimensional method of characteristics and used to simulate pressures radiated into the external flow field when a wavefront propagating along a duct reflects at a duct exit.

Two methods of combining the uniaxial and spherical methods have been considered. In the simpler of the two, the analyses are decoupled. First the uniaxial method is used to predict the flowrate history at the duct exit plane, based on an assumption of constant pressure in that plane. Then this history is used as the inner boundary condition of a simulation using the spherical method, enabling pressures and velocities to be predicted throughout the external flow field. This ensures conservation of mass between the two domains, but the pressure is strongly discontinuous. The inner boundary of the spherical domain is a spherical surface with the same total area as the duct cross-section. This is more reasonable than, for example, treating the external flow field as a monopole with its origin at the centroid of the duct exit plane.

The second method of combining the uniaxial and spherical analyses is coupled. An interface between the two domains satisfies conservation of energy as well as mass. It also ensures continuity of velocity, although the geometrical shape changes abruptly from plane to spherical. This interactive coupling achieves a good approximation to dynamic continuity as well as mass continuity.

It is envisaged that the coupled method will be of significant practical value during the early stages of an engineering design, enabling large numbers of comparisons to be simulated in cases where the alternative use of fully three-dimensional methods of analysis would be prohibitively expensive in time and human resources.

Appendix A. Liquid flow equations

The theoretical development presented in Section 2 is applicable to an ideal gas. For liquid flows, the relationship between changes in density and pressure is usually expressed as $\mathrm{d}p/\mathrm{d}\rho = K/\rho$, where K denotes a bulk modulus that may be

regarded as a constant for many practical purposes. In this case, $c^2 = \mathrm{d}p/\mathrm{d}\rho = K/\rho$ and Eqs. (2.3) and (2.4) may be expressed as:

$$\frac{\partial}{\partial t}(p) + u_r \frac{\partial}{\partial r}(p) + \frac{K}{r^2}\frac{\partial}{\partial r}\left(u_r r^2\right) = \frac{K}{\rho r^2} C \tag{A.1}$$

and

$$\frac{\partial}{\partial r}(p) + \frac{\rho}{r^2}\frac{\partial}{\partial t}\left(r^2 u_r\right) + \frac{\rho u_r}{r^2}\frac{\partial}{\partial r}\left(r^2 u_r\right) = 2\frac{\rho {u_r}^2}{r} + \frac{1}{r^2}(M - u_r C) \tag{A.2}$$

These two equations can be combined into a characteristic form, namely as a pair of ordinary differential equations:

$$\frac{d}{dt}(p) \pm \frac{\rho c^2}{r^2}\frac{d}{dt}\left(r^2 u_r\right) = \pm 2\frac{\rho c {u_r}^2}{r} + \frac{c}{r^2}[\pm M + (c \mp u_r)C] \tag{A.3}$$

that are valid in the directions

$$\frac{dr}{dt} = u_r \pm c \tag{A.4}$$

Appendix B. Flow field around a vibrating sphere

Consider the flow field outside a vibrating sphere of radius $r = a$. If the initial condition for all $r > a$ is a stationary fluid at uniform pressure p_0, the fluctuating component of the pressure field, namely $p' = p - p_0$, satisfies

$$r.p'\{r, t\} = \frac{1}{4\pi}\rho_0 \dot{Q}_a\{t - (r - a)/c_0\} \tag{B.1}$$

and the velocity field satisfies

$$r.u_r\{r, t\} = \frac{1}{4\pi}\left[\frac{\dot{Q}_a\{t - (r - a)/c_0\}}{c_0} + \frac{Q_a\{t - (r - a)/c_0\}}{r}\right] \tag{B.2}$$

where $p'\{r, t\}$ is applicable at any radius $r > a$ at the time t, ρ_0 and c_0 are the density and speed of sound of the ambient fluid. $Q_a\{t - (r - a)/c_0\}$ is the fluctuating volumetric flowrate at the surface $r = a$ at the earlier time $t - (r - a)/c_0$ (known as a 'retarded' time) and $\dot{Q}_a$ denotes the time rate of change of Q_a. The latter cannot be chosen arbitrarily: the velocity u_r has to satisfy a boundary condition at $r = a$. Accordingly, an analytical expression for Q_a is derived in Section B.1.

An important deduction from Eq. (B.1) is that the pressure at any radius r_2 and time t_2 can be deduced unambiguously from the pressure at any smaller radius $r_1 > a$ at an earlier time t_1. The simple relationship

$$r_2.p_2'\{r_2, t_2\} = r_1.p_1'\{r_1, t_1\} \tag{B.3}$$

applies between two points in space-time satisfying

$$t_2 - t_1 = (r_2 - r_1)/c_0 \tag{B.4}$$

Subject to satisfying Eq. (B.4), the choices of r_1 and t_1 are arbitrary. It is common to choose r_1 at the surface of the sphere, but the more general formulation expressed in Eqs. (B.3) and (B.4) has the advantage of highlighting similarities with the MOC equations.

Eq. (B.2) shows that the velocity has two components, one dependent on the acceleration at $r = a$ at the retarded time and the other dependent on the corresponding velocity. At sufficiently large radii, the second term may be neglected and so the pressure and velocity are almost in phase. In contrast, at sufficiently small radii, the second term can be dominant, in which case the pressure and velocity are up to 90° out of phase. These contrasting behaviours are conventionally termed far-field and near-field behaviour respectively. In the far field, the proportional change in flow area associated with small distances of wave propagation is small and so the local propagation approximates to that of uniaxial, one-dimensional behaviour.

B.1. General solution

The governing Eqs. (2.3) and (2.4) can be linearised ($\rho \approx \rho_0$, $c \approx c_0$, $\mathrm{Ma} = u_r/c_0 \ll 1$, $C = 0$, $M = 0$) and cast as second-order partial differential equations for $r\,p'$ and $r\,u_r$:

$$\frac{\partial^2 (rp')}{\partial t^2} - c_0^2 \frac{\partial^2 (rp')}{\partial r^2} = 0 \tag{B.5}$$

$$\frac{\partial^2 (r\,u_r)}{\partial t^2} - c_0^2 \frac{\partial^2 (r\,u_r)}{\partial r^2} + 2c_0^2 \frac{u_r}{r} = 0 \tag{B.6}$$

The equation for rp' is the standard wave equation, which allows solutions of the form:

$$rp' = F\{t - r/c_0\} \tag{B.7}$$

where F has unit kg/s^2. Note that, at large radii, the equation for ru_r also becomes the standard wave equation. The velocity u_r follows from p' via

$$\rho_0 \frac{\partial u_r}{\partial t} = -\frac{\partial p'}{\partial r} \tag{B.8}$$

Differentiation of $p' = F\{t - r/c_0\}/r$ with respect to r gives

$$\rho_0 \frac{\partial u_r}{\partial t} = \frac{1}{r^2} F\{t - r/c_0\} + \frac{1}{c_0\, r} \dot{F}\{t - r/c_0\} \tag{B.9}$$

If the velocity $u_r\{a,\ t\} = U_{r=a}\{t\}$ of the sphere's surface is a given function of time, then substitution of $r = a$ (*constant*) results in a linear first-order ordinary differential equation for F:

$$\dot{F}\{t^*\} + \frac{1}{t_0} F\{t^*\} = \rho_0\, c_0^2\, t_0\, \frac{\mathrm{d}U_{r=a}\{t\}}{\mathrm{d}t} \tag{B.10}$$

where $t^* = t - t_0$ and $t_0 = a\,/\,c_0$. The solution of Eq. (B.10) is

$$F\{t^*\} = \rho_0\, c_0^2\, t_0 \int_{-t_0}^{t^*} \mathrm{e}^{(\tilde{t} - t^*)/t_0} \frac{\mathrm{d}U_{r=a}\{\tilde{t} + t_0\}}{\mathrm{d}t} d\tilde{t} + C_1\, \mathrm{e}^{-t^*/t_0} \tag{B.11}$$

where $\tilde{t}$ is a dummy variable and the constant of integration $C_1 = 0$ if $F = 0$ for $t = 0$, and thus $F\{-t_0\} = 0$. The pressure histories at $r = a$, $r = 2a$ and $r = 3a$ shown in Figs. 7 and 8 follow from Eq. (B.7) as $p'\{a,\ t\} = F\{t - t_0\}\,/\,a$, $p'\{2a,\ t\} = F\{t - 2t_0\}\,/\,(2a)$ and $p'\{3a,\ t\} = F\{t - 3t_0\}\,/\,(3a)$, respectively. The acceleration is derived from Eqs. (B.7) and (B.8) as

$$\frac{\partial u_r}{\partial t}\{r,\ t\} = \frac{a}{r}\, \frac{\mathrm{d}U_{r=a}\{t - r/c_0 + t_0\}}{\mathrm{d}t} - \frac{r - a}{\rho_0\, a\, r^2}\, F\{t - r/c_0\} \tag{B.12}$$

and the velocity from subsequent time integration

$$u_r\{r,\ t\} = \frac{a}{r}\, U_{r=a}\{t - r/c_0 + t_0\} - \frac{r - a}{\rho_0\, a\, r^2} \int_0^t F\{\tilde{t} - r/c_0\}\, d\tilde{t} \tag{B.13}$$

Compare Eqs. (B.7) with Eq. (B.1) to see that for a "simple source" [23, p. 19]

$$F\{t - r/c_0\} = \frac{1}{4\pi} \rho_0\, \dot{Q}_a\{t - r/c_0 + t_0\} = \rho_0\, a^2\, \dot{U}_a\{t - r/c_0 + t_0\} \tag{B.14}$$

which is Eq. (B.10) when the derivative $\dot{F}$ is ignored, noting that $a^2 = c_0^2\, t_0^2$.

B.2. Single pulse sech{t}

When the flowrate Q induced by the sphere varies in a sufficiently simple manner, it can be possible to derive analytical expressions for the whole flow field $r > a$ at all times. In acoustics, an especially important case is a simple harmonic oscillation of velocity. Herein, the behaviour of a single pulse is more relevant and the chosen form is Eq. (4.1):

$$U_{r=a} = U_0\, \mathrm{sech}\left\{ \beta \left(\frac{t}{\tau} - 1 \right) \right\} \tag{B.15}$$

so that the sphere's acceleration and displacement are

$$\frac{dU_{r=a}}{dt} = \frac{\beta\, U_0\ \tanh\left\{ \beta \left(\frac{t}{\tau} - 1 \right) \right\}}{\tau\ \cosh\left\{ \beta \left(\frac{t}{\tau} - 1 \right) \right\}} \tag{B.16}$$

and

$$\int U_{r=a}\, dt = \frac{2\,\tau}{\beta} \left\{ \arctan\left(\mathrm{e}^{\beta \left(\frac{t}{\tau} - 1 \right)} \right) - \arctan\left(\mathrm{e}^{-\beta} \right) \right\} \tag{B.17}$$

The sech function is a smooth pulse roughly of width 10, see Fig. B.1, so that the duration of the scaled (and shifted) pulse (B.15) is about $10\,\tau/\beta$. Substitution of (B.16) into (B.11) gives an integral which, herein, is calculated numerically. However, fully symbolic solutions can be derived for the particular cases of $\tau/(\beta\, t_0)$ equal to 1, 2 and 3.

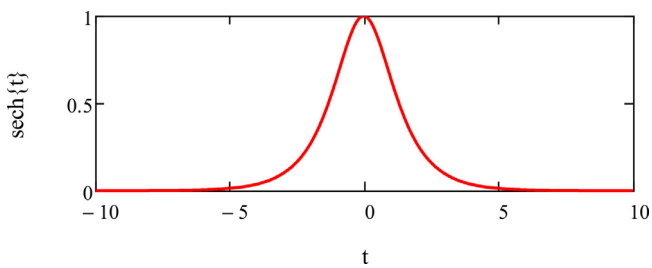

Fig. B.1. Sech pulse.

References

[1] G. Rudinger, The reflection of pressure waves of finite amplitude from an open end of a duct, J. Fluid Mech. 3 (1) (1957) 48–66.
[2] S.W. Rienstra, A gasdynamic-acoustic model of a bird scare gun, Mathematical modeling: case studies from industry, Eds.: Ellis Cumberbatch and Alistair Fitt, Cambridge University Press, 2001, pp. 253–269.
[3] A.D. Jones, G.L. Brown, Determination of two-stroke engine exhaust noise by the method of characteristics, J. Sound Vib. 82 (3) (1982) 305–327.
[4] T. Miyachi, Acoustic model of micro-pressure wave emission from a high-speed train tunnel, J. Sound Vib. 391 (2017) 127–152.
[5] P.C. Chou, H.A. Koenig, A unified approach to cylindrical and spherical elastic waves by method of characteristics, J. Appl. Mech.: Trans. ASME 33 (1) (1966) 159–167.
[6] J.B. Haddow, A. Mioduchowski, Analysis of expansion of spherical cavity in unbounded hyperelastic medium by method of characteristics, Acta Mech. 23 (3–4) (1975) 219–234.
[7] L. Olaosebikan, Vibration analysis of elastic spherical shells, Int. J. Eng. Sci. 24 (10) (1986) 1637–1654.
[8] N. Sumi, Y. Ito, The propagation and reflection of thermal stress waves in anisotropic nonhomogeneous hollow cylinders and spheres, Nucl. Eng. Des. 140 (2) (1993) 133–145.
[9] R. Kumar, B.S. Hundal, Symmetric wave propagation in a fluid-saturated incompressible porous medium, J. Sound Vib. 288 (1–2) (2005) 361–373.
[10] A. Prosperetti, A. Lezzi, Bubble dynamics in a compressible liquid, J. Fluid. Mech. 168 (1986) 457–478.
[11] C. Zhang, X. Li, C. Yang, A modified method of characteristics and its application in forward and inversion simulations of underwater explosion, AIP Adv. 6 (7) (2016) 075319.
[12] P.C. Chou, R.R. Karpp, S.L. Huang, Numerical calculation of blast waves by the method of characteristics, AIAA J. 5 (4) (1967) 618–623.
[13] H. Steiner, W. Gretler, T. Hirschler, Numerical solution for spherical laser-driven shock waves, Shock Waves 8 (3) (1998) 139–147.
[14] A.N. Kraiko, Rapid cylindrically and spherically symmetric strong compression of a perfect gas, J. App. Maths. Mech. 71 (5) (2007) 676–689.
[15] X. Li, C. Zhang, X. Wang, X. Hu, Numerical study of underwater shock wave by a modified method of characteristics, J. App. Phys. 115 (10) (2014) 104905.
[16] P.O.A.L. Davies, M.F. Harrison, Predictive acoustic modelling applied to the control of intake/exhaust noise of internal combustion engines, J. Sound Vib. 202 (2) (1997) 249–274.
[17] P.O.A.L. Davies, P.E. Doak, Spherical wave propagation in a conical pipe with mean flow, J. Sound Vib. 137 (2) (1990) 343–346.
[18] V.L. Streeter, E.B. Wylie, Two and three-dimensional fluid transients, J. Basic Eng.: Trans. ASME 90 (4) (1968) 501–510.
[19] A.E. Vardy, Reflections of step-wavefronts from perforated and flared tube extensions, J. Sound Vib. 59 (4) (1978) 577–589.
[20] H.M. Paynter, I.J. Busch-Vishniac, Remarks on Riemann's method of characteristics, J. Acoust. Soc. Amer. 84 (3) (1988) 813–821. Erratum: 85 (1989) 1784.
[21] G. Papadakis, New analytic solutions for wave propagation in flexible, tapered vessels with reference to mammalian arteries, J. Fluid. Mech. 689 (2011) 465–488.
[22] G. Papadakis, Wave propagation in tapered vessels: new analytic solutions that account for vessel distensibility and fluid compressibility, J. Press. Vessel Technol. 136 (2014) 014501.
[23] J. Lighthill, Waves in Fluids, Cambridge University Press, 1978 Sections 1.4, 1.11 and 2.14.
[24] S.W. Rienstra, A. Hirschberg, An Introduction to Acoustics, Eindhoven University of Technology, 2004. Sections 2.2, 6.2 and 6.7.
[25] G. Rudinger, On the reflection of shock waves from an open end of a duct, J. Appl. Phys. 26 (8) (1955) 933–981.
[26] J.M.B. Brown, A.E. Vardy, Reflections of pressure waves at tunnel portals, J. Sound Vib. 173 (1) (1994) 95–111.
[27] A.S. Lyrintzis, Review: the use of Kirchhoff's method in computational aeroacoustics, J. Fluids Eng. Trans. ASME 116 (4) (1994) 665–676.